

# Electrochemistry-Induced Restructuring of Tin-Doped Indium Oxide Nanocrystal Films of Relevance to CO<sub>2</sub> Reduction

To cite this article: Tawney A. Knecht *et al* 2021 *J. Electrochem. Soc.* **168** 126521

## Manuscript version: Accepted Manuscript

Accepted Manuscript is “the version of the article accepted for publication including all changes made as a result of the peer review process, and which may also include the addition to the article by IOP Publishing of a header, an article ID, a cover sheet and/or an ‘Accepted Manuscript’ watermark, but excluding any other editing, typesetting or other changes made by IOP Publishing and/or its licensors”

This Accepted Manuscript is © .



During the embargo period (the 12 month period from the publication of the Version of Record of this article), the Accepted Manuscript is fully protected by copyright and cannot be reused or reposted elsewhere.

As the Version of Record of this article is going to be / has been published on a subscription basis, this Accepted Manuscript will be available for reuse under a CC BY-NC-ND 3.0 licence after the 12 month embargo period.

After the embargo period, everyone is permitted to use copy and redistribute this article for non-commercial purposes only, provided that they adhere to all the terms of the licence <https://creativecommons.org/licenses/by-nc-nd/3.0>

Although reasonable endeavours have been taken to obtain all necessary permissions from third parties to include their copyrighted content within this article, their full citation and copyright line may not be present in this Accepted Manuscript version. Before using any content from this article, please refer to the Version of Record on IOPscience once published for full citation and copyright details, as permissions may be required. All third party content is fully copyright protected, unless specifically stated otherwise in the figure caption in the Version of Record.

View the [article online](#) for updates and enhancements.

**Electrochemistry-Induced Restructuring of Tin-Doped Indium Oxide Nanocrystal Films of Relevance to CO<sub>2</sub> Reduction**

Journal:	<i>Journal of The Electrochemical Society</i>
Manuscript ID	JES-105948.R1
Manuscript Type:	Research Paper
Date Submitted by the Author:	06-Dec-2021
Complete List of Authors:	Knecht, Tawney; University of Oregon, Chemistry and Biochemistry Boettcher, Shannon W. ; University of Oregon Hutchison, James; University of Oregon
Keywords:	carbon dioxide reduction, Electrocatalysis, restructuring

SCHOLARONE™  
Manuscripts

# Electrochemistry-Induced Restructuring of Tin-Doped Indium Oxide Nanocrystal Films of Relevance to CO<sub>2</sub> Reduction

Tawney A. Knecht, Shannon W. Boettcher,<sup>\*,z</sup> and James E. Hutchison<sup>z</sup>

Department of Chemistry and Biochemistry,

University of Oregon, Eugene, Oregon 97403, United States

<sup>\*</sup>Electrochemical Society Member.

<sup>z</sup>E-mail: [swb@uoregon.edu](mailto:swb@uoregon.edu); [hutch@uoregon.edu](mailto:hutch@uoregon.edu)

## ABSTRACT

The electrochemical reduction of CO<sub>2</sub> into fuels using renewable electricity presents an opportunity to utilize captured CO<sub>2</sub>. Electrocatalyst development has been the primary focus of research in this area. This is especially true at the nanoscale, where researchers have focused on understanding nanostructure-property relationships. However, electrocatalyst structure may evolve during operation. Indium- and tin-based oxides have been widely studied as electrocatalysts for CO<sub>2</sub> reduction to formate, but evolution of these catalysts during operation is not well-characterized. Here, we report the evolution of nanoscale structure of tin-doped indium oxide nanocrystals under CO<sub>2</sub> reduction conditions. We show that sparse monolayer nanocrystal films desorb from the electrode upon charging, but thicker nanocrystal films remain, likely due to increased number of physical contacts. Upon applying a cathodic voltage of -1.0 V vs RHE or greater, the original 10-nm diameter nanocrystals are no longer visible, and instead form a larger microstructural network. Elemental analysis suggests the network is an oxygen-deficient indium-tin metal alloy. We hypothesize that this morphological evolution is the result of nanocrystal sintering due to oxide reduction. These data provide insights into the morphological evolution tin-doped indium oxide nanocrystal electrocatalysts under reducing conditions and highlight the importance of post-electrochemical structural characterization of electrocatalysts.

## INTRODUCTION

The electrochemical reduction of CO<sub>2</sub> into hydrocarbon products utilizing renewable electricity is of technological and economic interest.<sup>1</sup> However, the high overpotentials required to drive the reaction, as well as the propensity to make a number of different products with poor selectivity has hindered commercialization.<sup>2-3</sup> Significant effort has been put into developing and understanding various electrocatalysts for the CO<sub>2</sub> reduction reaction (CO<sub>2</sub>RR).<sup>2-7</sup> Nanoscale electrocatalysts, which have higher surface areas and can have different properties from their bulk counterparts, are promising candidates and have been widely studied.<sup>8-17</sup> However, if size- and morphology-dependent properties are not maintained during the electrochemical reaction conditions, the unique catalytic activity of these materials may be lost. Further, elucidating structure-activity relationships and designing nanoscale structure to influence properties, becomes difficult. Thus, it is important to understand the stability and structural evolution of nanoscale catalysts under operating conditions to help enable rational catalyst design.

Indium- and tin-based oxides, including nanoparticles, have shown promise as selective CO<sub>2</sub>RR electrocatalysts for formate.<sup>12, 15, 18-25</sup> Extensive studies of these oxide catalysts has been done by both Bocarsly and Kanan and coworkers. They found that, despite the electrochemical reduction of the oxide to In and Sn metal, a metastable oxide persists under reducing conditions that is thought to be important for selective reduction of CO<sub>2</sub> to formate.<sup>18, 22, 26-29</sup> Huang et al. evaluated the size-dependent reactivity of In<sub>2</sub>O<sub>3</sub> nanoparticle catalysts, concluding that catalysts derived from 15 nm In<sub>2</sub>O<sub>3</sub> nanocubes exhibited superior formate selectivity compared to catalysts derived from smaller (5 nm) or larger (200 nm) In<sub>2</sub>O<sub>3</sub> structures.<sup>15</sup> However, a recent report from Pardo et al. demonstrated that indium-tin-oxide films undergo structural changes during CO<sub>2</sub>RR conditions, forming core-shell nanoparticles rich in indium oxide at the surface. Collectively,

1  
2  
3 these studies raise questions about the stability of these catalysts and the properties of the catalyst  
4 (i.e. size, morphology) that are contributing to the observed activity or selectivity.<sup>30</sup>  
5  
6  
7

8 The electrochemical restructuring of nanoscale CO<sub>2</sub>RR electrocatalysts under operating  
9 conditions has been previously reported using a variety of complementary *operando* techniques  
10 such as *in situ* transmission electron microscopy (TEM)<sup>10</sup>, *in situ* Raman spectroscopy<sup>31</sup>, and  
11 more.<sup>8, 10, 17, 31-33</sup> For example, Cu<sub>2</sub>O nanocubes were found to become more branched and form  
12 dendrites as a result of a dissolution-redeposition process occurring during CO<sub>2</sub> reduction.<sup>10</sup>  
13 Similar phenomena were seen with various Cu<sup>17, 31</sup> and Cu-alloy<sup>8, 33</sup> catalysts. Despite these  
14 studies, few reports have examined the evolution of In- and Sn-based CO<sub>2</sub>RR electrocatalysts.  
15  
16  
17  
18  
19  
20  
21  
22  
23  
24

25 There are several mechanisms by which nanoscale catalysts can restructure during the  
26 course of electrocatalysis.<sup>34-36</sup> A common form of restructuring is sintering, wherein nanocrystals  
27 coalesce through either surface diffusion or a ripening process (i.e. dissolution-redeposition)  
28 causing smaller nanocrystals are dissolved and redeposit as larger nanoparticles.<sup>34</sup> The degree of  
29 sintering depends upon how the nanocrystal-modified electrode is prepared. For instance, sintering  
30 can sometimes be prevented through the use of organic ligand modifiers or engineered supports  
31 with strong catalyst-support interactions.<sup>34</sup> Thus, the preparation method is an important  
32 consideration when evaluating the stability and structural evolution of nanoscale catalysts.  
33  
34  
35  
36  
37  
38  
39  
40  
41  
42  
43

44 Herein we report the stability and structural evolution of well-defined tin-doped indium  
45 oxide (ITO) nanocrystals under electrochemical CO<sub>2</sub>RR conditions. The nanocrystal films were  
46 fabricated in two different ways to evaluate the stability of the ITO nanocrystals on the electrode  
47 support and the mechanisms associated with the morphological changes. When a sparse monolayer  
48 of nanocrystals was deposited on the electrode, the nanocrystals desorbed from the electrode under  
49 electrochemically reductive conditions, presumably due to charging that leads to higher solubility.  
50  
51  
52  
53  
54  
55  
56  
57  
58  
59  
60

1  
2  
3 Thicker nanocrystal films (~150 nm), however, were found to adhere to the electrode substantially  
4 better allowing for CO<sub>2</sub>RR electrolyses conducted for up to 80 min. Chronoamperometry  
5 experiments were performed on ITO-nanocrystal-modified electrodes at different potentials for  
6 varying amounts of time. Structural characterization of the electrodes was performed before and  
7 after electrochemical experiments to investigate how the structure of the nanocrystals change as a  
8 function of potential and the amount of time that potential is applied. We discover that the original  
9 size, morphology, and composition of the ITO nanocrystals is not retained, with the initially well-  
10 defined ITO nanoparticle assemblies evolving into larger crystallites of an oxide-deficient  
11 indium/tin metal alloy. These results are important in the context of using tin/indium-based  
12 nanomaterials for CO<sub>2</sub>RR catalysis.  
13  
14  
15  
16  
17  
18  
19  
20  
21  
22  
23  
24  
25

## 26 27 **EXPERIMENTAL**

28  
29  
30 **Materials.** Indium(III) acetate (99.99%), tin(IV) acetate (99.95%), oleic acid (90%  
31 technical grade), and potassium bicarbonate (99.95%) were acquired from Sigma-Aldrich and used  
32 as received. Oleyl alcohol (85% technical grade) was acquired from Alfa Aesar and used as  
33 received. The boron-doped diamond (BDD) electrodes were acquired from Element Six.  
34  
35  
36  
37  
38  
39

40 **Nanocrystal Synthesis.** ITO nanocrystals were synthesized using a previously reported  
41 procedure.<sup>37</sup> Briefly, indium acetate (1.8 mmol) and tin acetate (0.2 mmol) were mixed in 4 mL of  
42 oleic acid and stirred under N<sub>2</sub>(g) at 150 °C for 1 h to form the metal-oleate precursor. This mixture  
43 was then injected into 13 mL of oleyl alcohol at 290 °C at a rate of 0.3 mL min<sup>-1</sup>. Oleate-stabilized  
44 nanocrystals were washed three times by dispersion in acetone followed by centrifugation (7000  
45 RPM for 5 min) and decanting the solvent.  
46  
47  
48  
49  
50  
51  
52  
53  
54  
55  
56  
57  
58  
59  
60

1  
2  
3       **Electrode fabrication.** To form a thin, sparse monolayer of ITO nanocrystals, BDD  
4 electrodes were submerged in a  $0.5 \text{ mg mL}^{-1}$  solution of ITO nanocrystals in toluene for 2 h. To  
5 form thicker ITO nanocrystal films, a  $50 \text{ mg/mL}$  solution of ITO nanocrystals in toluene was spin  
6 coated onto BDD electrodes by flooding the electrode with nanoparticle solution, then rotating at  
7 3000 rpm for 30 s. All electrodes were gently washed with toluene after nanocrystal  
8 deposition/assembly to remove any poorly adsorbed nanocrystals. The coated electrodes were then  
9 submerged in a 1 M solution of formic acid in acetonitrile for 1 h to remove the oleate ligands, and  
10 then gently rinsed with acetonitrile. Afterwards, electrodes were annealed in a tube furnace under  
11 forming gas at  $300 \text{ }^\circ\text{C}$  for 4 h to remove any absorbed formate.  
12  
13  
14  
15  
16  
17  
18  
19  
20  
21  
22  
23

24       **Electrochemical characterization.** A single-compartment three-electrode  
25 electrochemical cell consisting of the ITO-modified BDD working electrode, a Pt counter  
26 electrode, and an Ag/AgCl reference electrode (3 M NaCl), with aq.  $0.5 \text{ M KHCO}_3$  as the  
27 electrolyte was used for measurements. All electrodes were analyzed using cyclic voltammetry  
28 (CV) at a scan rate of  $100 \text{ mV s}^{-1}$ . CV and chronoamperometry (varying potentials and duration)  
29 were performed using a BioLogic SP300 potentiostat. All potentials were corrected for  
30 uncompensated series resistance, which was between  $7.0$  to  $9.0 \text{ } \Omega$  for all experiments. Prior to  
31 electrochemical experiments, the electrolyte was sparged with either Ar (99.999%) or  $\text{CO}_2$  (99.5%)  
32 for 30 min at a flow rate of 30 sccm, and then the gas was kept flowing in the headspace of the  
33 electrochemical cell for the duration of the experiments.  
34  
35  
36  
37  
38  
39  
40  
41  
42  
43  
44  
45  
46  
47

48       **Physical characterization.** The size and morphology of the synthesized colloidal  
49 nanocrystals were characterized using a FEI Tecnai Spirit transmission electron microscope  
50 (TEM) operating at 120 kV. Nanocrystals were deposited on lacey-carbon grids supported on 400  
51 mesh copper (Ted Pella) for TEM visualization. The size of the nanocrystals were ascertained  
52  
53  
54  
55  
56  
57  
58  
59  
60

1  
2  
3 using an Anton-Paar SAXSess small angle X-ray scattering (SAXS) instrument. The morphology  
4 of the nanocrystal films before and after electrochemical experiments was assessed using a FEI  
5 Helios Nanolab 600i scanning-electron microscope<sup>38</sup> equipped with a through-lens detector.  
6  
7 Energy-dispersive X-ray spectrometry (EDS) was performed using the same SEM instrument to  
8 evaluate the composition of certain films. X-ray photoelectron spectroscopy (XPS) was used to  
9 evaluate the composition of the nanocrystals, as well as assess the ITO nanocrystal content on the  
10 electrodes (Thermo Scientific ESCALAB 250). A Bruker 500 nuclear magnetic resonance (NMR)  
11 spectrometer was used for qualitative liquid product characterization.  
12  
13  
14  
15  
16  
17  
18  
19  
20  
21

## 22 **RESULTS AND DISCUSSION**

### 23 **Evaluation of electrochemical stability of ITO nanocrystal films on a carbon support.**

24  
25 The methods used to prepare the nanocrystal film on the electrode can affect the overall ability of  
26 electrocatalysts to catalyze the CO<sub>2</sub> reduction reaction, and several experimental parameters must  
27 be considered. When studying fundamental properties of nanocrystal electrocatalysts, an ideal  
28 platform consists of a conductive electrocatalyst deposited on a catalytically inactive, electrically  
29 conductive support such that the activity is due to the electrocatalyst alone and each catalyst  
30 particle is connected to the electrode with a low-resistance electrical path.<sup>15, 39-41</sup> We chose to  
31 investigate the evolution of nanoscale structure in tin-doped indium oxide (ITO) nanocrystals with  
32 10% tin doping because ITO is highly electrically conductive, and the activity and selectivity of  
33 In- and Sn-based oxide CO<sub>2</sub>RR catalysts are similar.<sup>25</sup> We synthesized the ITO nanocrystals using  
34 an established method (Figure 1) wherein a mixture of tin oleate and indium oleate in an excess of  
35 oleic acid is slowly injected via a syringe pump into oleyl alcohol at 290 °C.<sup>37, 42</sup> This yielded  
36 monodisperse ITO nanocrystals ~ 10 nm in diameter (see Fig. S1 for size analysis).  
37  
38  
39  
40  
41  
42  
43  
44  
45  
46  
47  
48  
49  
50  
51  
52  
53  
54  
55  
56  
57  
58  
59  
60

1  
2  
3 We considered several ways to fabricate the nanocrystal-modified electrodes. A boron-  
4 doped diamond (BDD) electrode was used as the electrode support due to its chemical  
5 stability/inertness and low intrinsic CO<sub>2</sub> reduction activity.<sup>43</sup> To functionalize the electrode, we  
6 considered using ionomer such as Nafion or Sustainion as a binder, as has been done in previous  
7 reports.<sup>27, 31, 44-46</sup> However, these ionomers have also been shown to alter the activity and selectivity  
8 of CO<sub>2</sub>RR catalysts,<sup>47</sup> the loadings are often variable,<sup>48</sup> the stability of these ionomers has not been  
9 studied, and ionomer/catalyst interactions are complex and poorly understood.<sup>49-50</sup> Taken together,  
10 the use of ionomer could make it difficult to attribute the electrode performance to electrocatalyst  
11 properties alone. Given these considerations, we aimed here to study ITO nanocrystals directly  
12 deposited onto the BDD electrode without ionomer.  
13  
14  
15  
16  
17  
18  
19  
20  
21  
22  
23  
24  
25

26  
27 Nanocrystal-modified electrodes were fabricated by submerging the BDD in a 0.5 mg/mL  
28 solution of oleate-stabilized nanocrystals to yield a sparse monolayer of nanocrystals on the  
29 surface. The electrode was submerged in 1 M formic acid in acetonitrile to remove the oleate  
30 ligands, and then annealed at 300 °C under a 95:5 mix of N<sub>2</sub>:H<sub>2</sub> to remove the formate ligands.<sup>51</sup>  
31 This preparation procedure has been previously shown by Fourier transform infrared (FTIR)  
32 analysis to successfully remove all ligands.<sup>51</sup> An SEM image of one electrode is shown in Fig. 1a,  
33 illustrating the uniform coverage achieved with well-defined nanoparticles.  
34  
35  
36  
37  
38  
39  
40  
41  
42

43  
44 Cyclic voltammetry (CV) was used to evaluate these electrodes. The 0.5 M KHCO<sub>3</sub>  
45 electrolyte was sparged with Ar prior to measurements. The potential was swept from the open  
46 circuit voltage to -1.3 V vs. RHE. The first CV cycle (Fig. 2b) showed a redox feature typical of  
47 the reduction and partial re-oxidation of In- and Sn-based oxides.<sup>18, 22</sup> We noticed that by the  
48 second CV cycle (Fig. 2b, inset) this redox feature diminished significantly, completely  
49 disappearing by the fourth cycle. The electrode was then characterized by SEM and XPS (Fig. 2c  
50  
51  
52  
53  
54  
55  
56  
57  
58  
59  
60

1  
2  
3 and 2d) without further electrochemical testing in order to evaluate electrode stability. The SEM  
4 showed fewer nanocrystals on the electrode, and only carbon and oxygen were detected by XPS.  
5  
6

7  
8 To explain the loss of nanocrystals from the electrode surface, we hypothesized that the  
9 nanocrystals either dissolved or desorbed. To determine the potential at which this happens, we  
10 fabricated a sparse ITO nanoparticle monolayer film (using the same procedure) on a gold-coated  
11 quartz crystal and used an electrochemical quartz crystal microbalance (EQCM) to monitor mass  
12 as we performed CVs at  $100 \text{ mV s}^{-1}$  in  $0.5 \text{ M KHCO}_3$ , cycling out to more negative potentials in  
13 subsequent cycles. The results are shown in Fig. 3a. The film mass was stable until approximately  
14  $-1.0 \text{ V vs RHE}$ , at which point nearly all of the mass was lost. This indicates that the loss of the  
15 nanocrystal film is dependent upon the applied potential.  
16  
17  
18  
19  
20  
21  
22  
23  
24  
25  
26

27 It is known that under reducing conditions in near-neutral potassium bicarbonate solutions,  
28 the local pH at the electrode surface increases as protons are consumed during the hydrogen  
29 evolution reaction,<sup>52-54</sup> so we wanted to determine whether the increased basicity caused loss of  
30 nanocrystals through dissolution. The same type of nanocrystal film as described above was  
31 prepared on a gold-plated QCM crystal and submerged in 50 mL of water. We then titrated in 10  
32 mL of concentrated KOH, up to pH = 14, while stirring in order to see if mass loss could be due  
33 to increasing alkalinity (Fig. 3b). Over the course of the titration, only 17% mass loss was  
34 observed. As a control, we repeated the experiment, instead titrating in concentrated  $\text{HNO}_3$ , which  
35 is known to dissolve ITO nanocrystals, and monitored the mass. We found a mass loss of 91%, as  
36 expected. We then soaked nanoparticle-modified electrodes in various pH solutions and compared  
37 the resulting SEM images to those taken of the as-prepared electrode (Fig. S2). In all cases, SEM  
38 images showed evidence of nanocrystals on the electrode, suggesting nanocrystals are not  
39 dissolving as a result of increased alkalinity.  
40  
41  
42  
43  
44  
45  
46  
47  
48  
49  
50  
51  
52  
53  
54  
55  
56  
57  
58  
59  
60

1  
2  
3 Taken together, these results indicate that increasing pH at the electrode surface does not  
4 lead to dissolution of the ITO nanocrystals from the electrode. We hypothesized that other  
5 mechanisms for nanocrystal loss could be the electrostatic repulsion of the nanoparticles from the  
6 electrode as a negative potential is applied,<sup>55</sup> or cathodic dissolution.<sup>56</sup> We found, however, that  
7 when starting with a thicker (~150 nm) nanocrystal film (detailed below), the nanocrystals remain  
8 on the electrode, suggesting that cathodic dissolution is unlikely. Thus, our evidence suggests that,  
9 for sub-monolayer films, the nanocrystals are desorbing because they become more soluble as they  
10 become negatively charged. Charge-induced increases in solubility are common in gold  
11 nanoparticles, for example.<sup>57</sup> It has been reported that it is necessary to crosslink gold nanoparticles  
12 to prevent their desorption during electrochemical analysis because the non-crosslinked particles  
13 became soluble when charged.<sup>57</sup>

### 29 ***Evolution of morphology of nanocrystal films***

31  
32 An alternative electrode fabrication procedure resulting in insoluble films was needed to  
33 study the structural evolution of ITO nanocrystals under electrochemically reducing conditions.  
34 Another way to produce ITO nanocrystal films has been reported<sup>51</sup> wherein a thicker film is made  
35 by spin coating a 50 mg/mL solution of ITO nanocrystals in toluene onto a substrate, soaking in a  
36 1 M formic acid solution, and annealing at 300 °C to remove remaining formate ligands. The  
37 resulting films were ~ 150 nm thick, with a mass loading of ~ 0.1 mg cm<sup>-2</sup>. We hypothesized that  
38 the higher mass loading of ITO nanocrystals, along with the annealing step, would prevent the  
39 desorption by providing more physical/chemical contact points to each individual nanoparticle or  
40 by crosslinking between oleate ligands that were not fully removed from the film.<sup>58-60</sup>

41  
42 We spin coated the nanocrystals onto a BDD substrate using the above procedure, and then  
43 conducted four CV cycles from open circuit (~ 1.48 V vs RHE) to -1.1 V vs RHE in Ar-saturated  
44  
45  
46  
47  
48  
49  
50  
51  
52  
53  
54  
55  
56  
57  
58  
59  
60

1  
2  
3 0.5 M KHCO<sub>3</sub> electrolyte (see Fig. S3). It appears from Fig. S3 that the appearance of the cathodic  
4 wave is predicated on a previous sweep to potentials more negative of -1.1 V vs RHE where In<sup>0</sup> is  
5 formed, followed by its re-oxidation upon the positive sweep. This is evidenced by the lack of a  
6 cathodic wave during the first CV cycle, but a clear cathodic wave on the second and third CV  
7 cycles. SEM characterization of the as-deposited nanocrystals (Fig. 4a) and of the electrode after  
8 performing four CV cycles (Fig. 4b) indicate that the ITO nanocrystal film remains on the  
9 electrode.  
10  
11  
12  
13  
14  
15  
16  
17  
18

19  
20 Cyclic voltammetry and chronoamperometry were used to evaluate the ITO nanocrystal  
21 films for CO<sub>2</sub>RR. The CVs (Fig. S3) were performed in both Ar- and CO<sub>2</sub>-sparged electrolyte. The  
22 voltammetry did not indicate higher current densities under CO<sub>2</sub>, but previous reports have  
23 demonstrated that while total reductive current may be suppressed in some cases, CO<sub>2</sub>RR products  
24 are often found.<sup>29, 41, 61</sup> Chronoamperometry was then performed at -0.8, -0.9, and -1.1 V vs RHE  
25 in CO<sub>2</sub>-saturated electrolyte (see Fig. S5) for 80 min each on three separate electrodes. NMR  
26 spectra taken of the electrolyte showed the presence of formate (Fig. S4), which indicated that CO<sub>2</sub>  
27 reduction was indeed occurring at these potentials, although this particular study is not focused on  
28 the product speciation.  
29  
30  
31  
32  
33  
34  
35  
36  
37  
38  
39  
40

41 We characterized the electrodes after the chronoamperometry experiments using SEM  
42 (Fig. 5) and found that the ITO nanocrystal films underwent significant morphological change.  
43 The 10-nm-diameter nanocrystals in Fig. 5a were no longer distinguishable on electrodes that had  
44 undergone electrochemical analysis, and instead larger agglomerates between ~400 nm to several  
45 microns were seen (Fig. 5b-d).  
46  
47  
48  
49  
50  
51

52  
53 Next, we studied how long a potential must be applied before the morphology of the  
54 nanocrystal film changed. We performed chronoamperometry at -1.1 V vs RHE for 5 min and for  
55  
56  
57  
58  
59  
60

1  
2  
3 25 min in CO<sub>2</sub>-sparged 0.5 M KHCO<sub>3</sub> (see Fig. S6), and evaluated the morphology by SEM. Even  
4  
5 after applying a potential for 5 min, larger, micron-sized particles were present on the electrode.  
6  
7 Although the sizes and shapes of the particles varied, they were generally larger after 25 min  
8  
9 compared to 5 min. These particles were also analyzed by SEM-EDS (Fig. S7 and Table S1) and  
10  
11 found to have little oxygen content, suggesting that the particles were reduced to an In/Sn metal  
12  
13 alloy. Some particles even appeared faceted at the micron scale (Figure 6b). We also performed  
14  
15 chronoamperometry using a QCM to monitor mass as a function of time in 0.5 M KHCO<sub>3</sub> at -1.1  
16  
17 V vs RHE and found that the mass of the In<sup>0</sup>/Sn<sup>0</sup> film was stable over the 30 min duration of the  
18  
19 experiment (Fig. S8).  
20  
21  
22  
23

24  
25 These results suggest that the nanoparticles are coalescing after reduction to metallic  
26  
27 species. It is likely that all of the nanocrystals are getting reduced as nanocrystal film conductivity  
28  
29 measurements conducted by Crockett et al. showed that nanocrystals in the films are electrically  
30  
31 well-connected to one another.<sup>51</sup> One mechanism that could be occurring is dissolution and  
32  
33 redeposition, wherein the In and Sn dissolve, producing In<sup>3+</sup> and Sn<sup>4+</sup> species that are subsequently  
34  
35 re-deposited as In and Sn metal onto the electrode surface. While this process has been observed  
36  
37 with ITO films under acidic conditions,<sup>36</sup> the solubility of In and Sn are low under the neutral-to-  
38  
39 basic conditions tested in the present study. Thus, it is reasonable to conclude that this type of  
40  
41 ripening is not likely occurring in this system.  
42  
43  
44  
45

46  
47 We thus hypothesize that the restructuring is due to diffusion of zero-valent In and Sn  
48  
49 adatoms. In the oxide form, ITO has a strong cohesive energy, and thus a high adatom diffusion  
50  
51 barrier.<sup>62</sup> On the contrary, both In<sup>0</sup> and Sn<sup>0</sup> have low cohesive energies, enabling facile diffusion  
52  
53 of adatoms.<sup>62-64</sup> This is consistent with previous studies investigating the mobility of In and Sn  
54  
55 adatoms.<sup>63-67</sup> For example, Wagner et al. found that under reducing conditions, In<sub>2</sub>O<sub>3</sub> was partially  
56  
57  
58  
59  
60

1  
2  
3 reduced and In adatoms were formed, which were able to diffuse across the surface.<sup>66</sup> Similarly,  
4  
5 Morris et al. studied the surface diffusion of In on a W surface and found that the activation energy  
6  
7 for diffusion decreased as the surface coverage of In increased.<sup>64</sup> Given this information, we  
8  
9 conclude that the reduction to In and Sn metal enables surface diffusion of adatoms, which then  
10  
11 coalesce to minimize surface energy.  
12  
13  
14

15 One interesting observation is that at shorter times of an applied potential (Fig. 6), the  
16  
17 generated microparticles appear faceted and crystalline. At longer times, there is a more-  
18  
19 agglomerated microscale network. It is possible that as a negative potential is applied for a longer  
20  
21 period of time, more and more of the film gets reduced, allowing for more In and Sn adatoms to  
22  
23 diffuse along the surface and coalesce with existing structures.  
24  
25  
26

## 27 CONCLUSION

28  
29  
30 We evaluated how applying cathodic potentials affect the stability and morphology of ITO  
31  
32 nanocrystal films. Sparse monolayer nanocrystal films are not stable at highly cathodic potentials  
33  
34 (more negative of -1.1 V vs RHE) as the nanocrystals are no longer present on the electrode after  
35  
36 a cathodic bias is applied. This phenomenon was found to be potential-dependent and we conclude  
37  
38 that it is due to increased solubility of the reductively charged nanoparticles as well as electrostatic  
39  
40 repulsion between the ITO nanocrystals and the carbon electrode. Thicker nanocrystal films were  
41  
42 found to be more stable and remain on the electrode upon cathodic polarization, but significant  
43  
44 morphology and composition changes were observed. The ITO was found to be converted to a  
45  
46 reduced In-Sn metal alloy, and the 10 nm nanocrystals were no longer distinguishable as they had  
47  
48 formed a larger microscale network. We hypothesize this is due to increased diffusion of In<sup>0</sup> and  
49  
50 Sn<sup>0</sup> adatoms, which subsequently coalesce.  
51  
52  
53  
54  
55  
56  
57  
58  
59  
60

1  
2  
3 These findings have implications in the field of nanoscale electrochemical CO<sub>2</sub> reduction  
4 catalysts. For example, White et al. compared the activity of In<sub>2</sub>O<sub>3</sub>, In(OH)<sub>3</sub>, and In nanoparticles,  
5  
6 and Huang et al. compared the size-dependent activity of various In<sub>2</sub>O<sub>3</sub> nanoparticles for CO<sub>2</sub>RR;  
7  
8 such restructuring may in fact be occurring in those systems as well.<sup>15, 27</sup> As such, this study  
9  
10 highlights the necessity of post-electrochemical surface characterization in order to fully  
11  
12 understand electrocatalyst structure.  
13  
14  
15  
16  
17  
18  
19  
20  
21  
22

## 23 ACKNOWLEDGEMENTS

24  
25  
26 This work was supported by the National Science Foundation through CHE-1610675. S.W.B  
27  
28 acknowledges support for his contributions from the Liquid Sunlight Alliance, a U.S. Department  
29  
30 of Energy, Office of Basic Energy Sciences, Fuels from Sunlight Hub under Award Number DE-  
31  
32 SC0021266. The project made use of CAMCOR facilities supported by grants from the W. M.  
33  
34 Keck Foundation, the M. J. Murdock Charitable Trust, ONAMI, the Air Force Research  
35  
36 Laboratory (FA8650-05-1-5041), the National Science Foundation (0923577 and 0421086), and  
37  
38 the University of Oregon.  
39  
40  
41  
42  
43  
44  
45

## 46 REFERENCES

- 47  
48  
49 1. Lee, M.-Y.; Park, K. T.; Lee, W.; Lim, H.; Kwon, Y.; Kang, S., Current achievements and  
50  
51 the future direction of electrochemical CO<sub>2</sub> reduction: A short review. *Angew. Chem. Int. Ed.*  
52  
53 **2019**, *50* (8), 769-815.  
54  
55  
56  
57  
58  
59  
60

- 1  
2  
3 2. Ting, L. R. L.; Yeo, B. S., Recent advances in understanding mechanisms for the  
4 electrochemical reduction of carbon dioxide. *Curr. Opin. Electrochem.* **2018**, *8*, 126-134.  
5  
6
- 7  
8  
9 3. Zhang, W.; Hu, Y.; Ma, L.; Zhu, G.; Wang, Y.; Xue, X.; Chen, R.; Yang, S.; Jin, Z.,  
10 Progress and Perspective of Electrocatalytic CO<sub>2</sub> Reduction for Renewable Carbonaceous Fuels  
11 and Chemicals. *Adv. Sci.* **2018**, *5* (1).  
12  
13
- 14  
15  
16 4. Gunasekar, G. H.; Park, K.; Jung, K. D.; Yoon, S., Recent developments in the catalytic  
17 hydrogenation of CO<sub>2</sub> to formic acid/formate using heterogeneous catalysts. *Inorg. Chem. Front.*  
18 **2016**, *3* (7), 882-895.  
19  
20  
21
- 22  
23  
24 5. Sun, Z.; Ma, T.; Tao, H.; Fan, Q.; Han, B., Fundamentals and Challenges of  
25 Electrochemical CO<sub>2</sub> Reduction Using Two-Dimensional Materials. *Chem* **2017**, *3* (4), 560-587.  
26  
27  
28
- 29  
30 6. Zheng, T.; Jiang, K.; Wang, H., Recent Advances in Electrochemical CO<sub>2</sub>-to-CO  
31 Conversion on Heterogeneous Catalysts. *Adv.* **2018**, *30* (48).  
32  
33  
34
- 35  
36 7. Zhu, D. D.; Liu, J. L.; Qiao, S. Z., Recent Advances in Inorganic Heterogeneous  
37 Electrocatalysts for Reduction of Carbon Dioxide. *Adv.* **2016**, *28* (18), 3423-3452.  
38  
39  
40
- 41 8. Longfei Wu; E. Kolmeijer, K.; Yue Zhang; Hongyu An; Sven Arnouts; Sara Bals;  
42 Thomas Altantzis; P. Hofmann, J.; Figueiredo, Marta C.; M. Hensen, E. J.; M. Weckhuysen, B.;  
43 Stam, Ward v. d., Stabilization effects in binary colloidal Cu and Ag nanoparticle electrodes under  
44 electrochemical CO<sub>2</sub> reduction conditions. *Nanoscale* **2021**, *13* (9), 4835-4844.  
45  
46  
47  
48  
49  
50
- 51 9. Zhang, S.; Kang, P.; Meyer, T. J., Nanostructured tin catalysts for selective electrochemical  
52 reduction of carbon dioxide to formate. *J. Am. Chem. Soc.* **2014**, *136* (5), 1734-1737.  
53  
54  
55  
56  
57  
58  
59  
60

- 1  
2  
3 10. Arán-Ais, R. M.; Rizo, R.; Grosse, P.; Algara-Siller, G.; Dembélé, K.; Plodinec, M.;  
4 Lunkenbein, T.; Chee, S. W.; Cuenya, B. R., Imaging electrochemically synthesized Cu<sub>2</sub>O cubes  
5 and their morphological evolution under conditions relevant to CO<sub>2</sub> electroreduction. *Nat.*  
6  
7  
8  
9  
10 *Commun.* **2020**, *11* (1), 1-8.  
11  
12  
13 11. Daiyan, R.; Lu, X.; Saputera, W. H.; Ng, Y. H.; Amal, R., Highly Selective Reduction of  
14 CO<sub>2</sub> to Formate at Low Overpotentials Achieved by a Mesoporous Tin Oxide Electrocatalyst. *ACS*  
15  
16 *Sustain. Chem. Eng.* **2018**, *6* (2), 1670-1679.  
17  
18  
19  
20  
21 12. Ding, C.; Li, A.; Lu, S. M.; Zhang, H.; Li, C., In Situ Electrodeposited Indium Nanocrystals  
22 for Efficient CO<sub>2</sub> Reduction to CO with Low Overpotential. *ACS Catal.* **2016**, *6* (10), 6438-6443.  
23  
24  
25  
26  
27 13. Fu, W.; Liu, Z.; Wang, T.; Liang, J.; Duan, S.; Xie, L.; Han, J.; Li, Q., Promoting C<sub>2</sub>+  
28  
29 Production from Electrochemical CO<sub>2</sub> Reduction on Shape-Controlled Cuprous Oxide  
30  
31 Nanocrystals with High-Index Facets. *ACS Sustain. Chem. Eng.* **2020**, *8* (40), 15223-15229.  
32  
33  
34  
35 14. Gao, D.; Zhou, H.; Wang, J.; Miao, S.; Yang, F.; Wang, G.; Wang, J.; Bao, X., Size-  
36  
37 Dependent Electrocatalytic Reduction of CO<sub>2</sub> over Pd Nanoparticles. *J. Am. Chem. Soc.* **2015**, *137*  
38  
39 (13), 4288-4291.  
40  
41  
42  
43 15. Huang, Y.; Mao, X.; Yuan, G.; Zhang, D.; Pan, B.; Deng, J.; Shi, Y.; Han, N.; Li, C.;  
44  
45 Zhang, L.; Wang, L.; He, L.; Li, Y.; Li, Y., Size-Dependent Selectivity of Electrochemical CO<sub>2</sub>  
46  
47 Reduction on Converted In<sub>2</sub>O<sub>3</sub> Nanocrystals. *Angew. Chem. Int. Ed.* **2021**, *60* (29), 15844-15848.  
48  
49  
50  
51 16. Kumar, B.; Atla, V.; Brian, J. P.; Kumari, S.; Nguyen, T. Q.; Sunkara, M.; Spurgeon, J.  
52  
53 M., Reduced SnO<sub>2</sub> Porous Nanowires with a High Density of Grain Boundaries as Catalysts for  
54  
55  
56  
57  
58  
59  
60

1  
2  
3 Efficient Electrochemical CO<sub>2</sub>-into-HCOOH Conversion. *Angew. Chem. Int. Ed.* **2017**, *56* (13),  
4  
5 3645-3649.  
6  
7

8  
9 17. Loiudice, A.; Lobaccaro, P.; Kamali, E. A.; Thao, T.; Huang, B. H.; Ager, J. W.; Buonsanti,  
10  
11 R., Tailoring Copper Nanocrystals towards C<sub>2</sub> Products in Electrochemical CO<sub>2</sub> Reduction.  
12  
13 *Angew. Chem. Int. Ed.* **2016**, *55* (19), 5789-5792.  
14  
15

16  
17 18. Baruch, M. F.; Pander, J. E.; White, J. L.; Bocarsly, A. B., Mechanistic Insights into the  
18  
19 Reduction of CO<sub>2</sub> on Tin Electrodes using in Situ ATR-IR Spectroscopy. *ACS Catal.* **2015**, *5* (5),  
20  
21 3148-3156.  
22  
23

24  
25 19. Cui, C.; Han, J.; Zhu, X.; Liu, X.; Wang, H.; Mei, D.; Ge, Q., Promotional effect of surface  
26  
27 hydroxyls on electrochemical reduction of CO<sub>2</sub> over SnOx/Sn electrode. *J. Catal.* **2016**, *343*, 257-  
28  
29 265.  
30  
31

32  
33 20. Gu, J.; Héroguel, F.; Luterbacher, J.; Hu, X., Densely Packed, Ultra Small SnO  
34  
35 Nanoparticles for Enhanced Activity and Selectivity in Electrochemical CO<sub>2</sub> Reduction. *Angew.*  
36  
37 *Chem. Int. Ed.* **2018**, *57* (11), 2943-2947.  
38  
39

40  
41 21. Han, N.; Ding, P.; He, L.; Li, Y.; Li, Y., Promises of Main Group Metal-Based  
42  
43 Nanostructured Materials for Electrochemical CO<sub>2</sub> Reduction to Formate. *Adv. Energy Mater.*  
44  
45 **2020**, *10* (11), 1902338-1902338.  
46  
47

48  
49 22. Detweiler, Z. M.; White, J. L.; Bernasek, S. L.; Bocarsly, A. B., Anodized indium metal  
50  
51 electrodes for enhanced carbon dioxide reduction in aqueous electrolyte. *Langmuir* **2014**, *30* (25),  
52  
53 7593-7600.  
54  
55  
56  
57  
58  
59  
60

- 1  
2  
3 23. Ghuman, K. K.; Wood, T. E.; Hoch, L. B.; Mims, C. A.; Ozin, G. A.; Singh, C. V.,  
4  
5 Illuminating CO<sub>2</sub> reduction on frustrated Lewis pair surfaces: Investigating the role of surface  
6  
7 hydroxides and oxygen vacancies on nanocrystalline In<sub>2</sub>O<sub>3-x</sub>(OH)<sub>y</sub>. *Phys. Chem. Chem. Phys.*  
8  
9 **2015**, *17* (22), 14623-14635.  
11  
12  
13 24. Hegner, R.; Rosa, L. F. M.; Harnisch, F., Electrochemical CO<sub>2</sub> reduction to formate at  
14  
15 indium electrodes with high efficiency and selectivity in pH neutral electrolytes. *Appl. Catal. B.*  
16  
17 **2018**, *238*, 546-556.  
19  
20  
21 25. Lai, Q.; Yang, N.; Yuan, G., Highly efficient In–Sn alloy catalysts for electrochemical  
22  
23 reduction of CO<sub>2</sub> to formate. *Electrochem. Commun.* **2017**, *83*, 24-27.  
24  
25  
26  
27 26. Detweiler, Z. M.; Wulfsberg, S. M.; Frith, M. G.; Bocarsly, A. B.; Bernasek, S. L., The  
28  
29 oxidation and surface speciation of indium and indium oxides exposed to atmospheric oxidants.  
30  
31 *Surf. Sci.* **2016**, *648*, 188-195.  
32  
33  
34  
35 27. White, J. L.; Bocarsly, A. B., Enhanced Carbon Dioxide Reduction Activity on Indium-  
36  
37 Based Nanoparticles. *J. Electrochem. Soc.* **2016**, *163* (6), H410-H416.  
38  
39  
40  
41 28. Chen, Y.; Kanan, M. W., Tin oxide dependence of the CO<sub>2</sub> reduction efficiency on tin  
42  
43 electrodes and enhanced activity for tin/tin oxide thin-film catalysts. *J. Am. Chem. Soc.* **2012**, *134*  
44  
45 (4), 1986-1989.  
46  
47  
48  
49 29. Pander, J. E.; Ren, D.; Huang, Y.; Loo, N. W. X.; Hong, S. H. L.; Yeo, B. S., Understanding  
50  
51 the Heterogeneous Electrocatalytic Reduction of Carbon Dioxide on Oxide-Derived Catalysts.  
52  
53 *ChemElectroChem* **2018**, *5* (2), 219-237.  
54  
55  
56  
57  
58  
59  
60

- 1  
2  
3 30. Pérez, L. C. P.; Teschner, D.; Willinger, E.; Guiet, A.; Driess, M.; Strasser, P.; Fischer, A.,  
4 In Situ Formed “Sn<sub>1-x</sub>In<sub>x</sub>@In<sub>1-y</sub>Sn<sub>y</sub>O<sub>z</sub>” Core@Shell Nanoparticles as Electrocatalysts for CO<sub>2</sub>  
5 Reduction to Formate. *Adv. Funct. Mater.* **2021**, 2103601-2103601.  
6  
7  
8  
9  
10  
11 31. Xu, Z.; Wu, T.; Cao, Y.; Chen, C.; Zeng, X.; Lin, P.; Zhao, W. W., Dynamic restructuring  
12 induced Cu nanoparticles with ideal nanostructure for selective multi-carbon compounds  
13 production via carbon dioxide electroreduction. *J. Catal.* **2020**, 383, 42-50.  
14  
15  
16  
17  
18  
19 32. Wu, Z.; Huang, L.; Liu, H.; Wang, H., Element-Specific Restructuring of Anion- and  
20 Cation-Substituted Cobalt Phosphide Nanoparticles under Electrochemical Water-Splitting  
21 Conditions. *ACS Catal.* **2019**, 9 (4), 2956-2961.  
22  
23  
24  
25  
26  
27 33. Weng, Z.; Zhang, X.; Wu, Y.; Huo, S.; Jiang, J.; Liu, W.; He, G.; Liang, Y.; Wang, H.,  
28 Self-Cleaning Catalyst Electrodes for Stabilized CO<sub>2</sub> Reduction to Hydrocarbons. *Angew. Chem.*  
29 *Int. Ed.* **2017**, 56 (42), 13135-13139.  
30  
31  
32  
33  
34  
35 34. Goodman, E. D.; Schwalbe, J. A.; Cargnello, M., Mechanistic Understanding and the  
36 Rational Design of Sinter-Resistant Heterogeneous Catalysts. *ACS Catal.* **2017**, 7 (10), 7156-7173.  
37  
38  
39  
40  
41 35. Geiger, S.; Kasian, O.; Mingers, A. M.; Mayrhofer, K. J. J.; Cherevko, S., Stability limits  
42 of tin-based electrocatalyst supports. *Sci. Rep.* **2017**, 7 (1).  
43  
44  
45  
46 36. Huang, C. A.; Li, K. C.; Tu, G. C.; Wang, W. S., The electrochemical behavior of tin-  
47 doped indium oxide during reduction in 0.3 M hydrochloric acid. *Electrochim. Acta* **2003**, 48 (24),  
48 3599-3605.  
49  
50  
51  
52  
53  
54  
55  
56  
57  
58  
59  
60

- 1  
2  
3 37. Jansons, A. W.; Hutchison, J. E., Continuous Growth of Metal Oxide Nanocrystals:  
4 Enhanced Control of Nanocrystal Size and Radial Dopant Distribution. *ACS Nano* **2016**, *10* (7),  
5 6942-6951.  
6  
7  
8  
9  
10  
11 38. Sweeney, S. W.; Roseman, G.; Deming, C. P.; Wang, N.; Nguyen, T. A.; Millhauser, G.  
12 L.; Chen, S., Impacts of oxygen vacancies on the electrocatalytic activity of AuTiO<sub>2</sub>  
13 nanocomposites towards oxygen reduction. *Int. J. Hydrog.* **2016**, *41* (40), 18005-18014.  
14  
15  
16  
17  
18  
19 39. Korotcenkov, G.; Brinzari, V.; Ivanov, M.; Cerneavschi, A.; Rodriguez, J.; Cirera, A.;  
20 Cornet, A.; Morante, J., Structural stability of indium oxide films deposited by spray pyrolysis  
21 during thermal annealing. *Thin Solid Films* **2005**, *479* (1-2), 38-51.  
22  
23  
24  
25  
26  
27 40. Köstlin, H.; Jost, R.; Lems, W., Optical and electrical properties of doped In<sub>2</sub>O<sub>3</sub> films.  
28 *Phys. Status Solidi* **1975**, *29* (1), 87-93.  
29  
30  
31  
32 41. Larrazábal, G. O.; Martín, A. J.; Mitchell, S.; Hauert, R.; Pérez-Ramírez, J., Synergistic  
33 effects in silver–indium electrocatalysts for carbon dioxide reduction. *J. Catal.* **2016**, *343*, 266-  
34 277.  
35  
36  
37  
38  
39  
40 42. Jansons, A. W.; Koskela, K. M.; Crockett, B. M.; Hutchison, J. E., Transition Metal-Doped  
41 Metal Oxide Nanocrystals: Efficient Substitutional Doping through a Continuous Growth Process.  
42 *Chem. Mater.* **2017**, *29* (19), 8167-8176.  
43  
44  
45  
46  
47  
48 43. Verlato, E.; Barison, S.; Einaga, Y.; Fasolin, S.; Musiani, M.; Nasi, L.; Natsui, K.; Paolucci,  
49 F.; Valenti, G., CO<sub>2</sub> reduction to formic acid at low overpotential on BDD electrodes modified  
50 with nanostructured CeO<sub>2</sub>. *J. Mater. Chem.* **2019**, *7* (30), 17896-17905.  
51  
52  
53  
54  
55  
56  
57  
58  
59  
60

- 1  
2  
3 44. Wu, Y.; Cao, S.; Hou, J.; Li, Z.; Zhang, B.; Zhai, P.; Zhang, Y.; Sun, L., Rational Design  
4 of Nanocatalysts with Nonmetal Species Modification for Electrochemical CO<sub>2</sub> Reduction. *Adv.*  
5  
6 *Energy Mater.* **2020**, *10* (29), 2000588-2000588.  
7  
8  
9  
10  
11 45. Yuan, J.; Zhang, J. J.; Yang, M. P.; Meng, W. J.; Wang, H.; Lu, J. X., CuO nanoparticles  
12 supported on TiO<sub>2</sub> with high efficiency for CO<sub>2</sub> electrochemical reduction to ethanol. *Catalysts*  
13  
14 **2018**, *8* (4), 171-171.  
15  
16  
17  
18  
19 46. Yuan, J.; Liu, L.; Guo, R. R.; Zeng, S.; Wang, H.; Lu, J. X., Electroreduction of CO<sub>2</sub> into  
20 ethanol over an active catalyst: Copper supported on Titania. *Catalysts* **2017**, *7* (7), 220-220.  
21  
22  
23  
24 47. Koshy, D. M.; Akhade, S. A.; Shugar, A.; Abiose, K.; Shi, J.; Liang, S.; Oakdale, J. S.;  
25 Weitzner, S. E.; Varley, J. B.; Duoss, E. B.; Baker, S. E.; Hahn, C.; Bao, Z.; Jaramillo, T. F.,  
26 Chemical Modifications of Ag Catalyst Surfaces with Imidazolium Ionomers Modulate H<sub>2</sub>  
27 Evolution Rates during Electrochemical CO<sub>2</sub> Reduction. *J. Am. Chem. Soc.* **2021**.  
28  
29  
30  
31  
32  
33  
34 48. Yang, Z.; Fujigaya, T.; Nakashima, N., Homogeneous coating of ionomer on  
35 electrocatalyst assisted by polybenzimidazole as an adhesive layer and its effect on fuel cell  
36 performance. *J. Power Sources* **2015**, *300*, 175-181.  
37  
38  
39  
40  
41  
42 49. Artyushkova, K.; Workman, M. J.; Matanovic, I.; Dzara, M. J.; Ngo, C.; Pylypenko, S.;  
43 Serov, A.; Atanassov, P., Role of Surface Chemistry on Catalyst/Ionomer Interactions for  
44 Transition Metal–Nitrogen–Carbon Electrocatalysts. *ACS Appl. Energy Mater.* **2018**, *1* (1), 68-77.  
45  
46  
47  
48  
49  
50 50. Berlinger, S. A.; McCloskey, B. D.; Weber, A. Z., Probing Ionomer Interactions with  
51 Electrocatalyst Particles in Solution. *ACS Energy Lett.* **2021**, *6* (6), 2275-2282.  
52  
53  
54  
55  
56  
57  
58  
59  
60

- 1  
2  
3 51. Crockett, B. M.; Jansons, A. W.; Koskela, K. M.; Sharps, M. C.; Johnson, D. W.;  
4  
5 Hutchison, J. E., Influence of Nanocrystal Size on the Optoelectronic Properties of Thin, Solution-  
6  
7 Cast Sn-Doped In<sub>2</sub>O<sub>3</sub> Films. *Chem. Mater.* **2019**, *31* (9), 3370-3380.  
8  
9  
10  
11 52. Burdyny, T.; Smith, W. A., CO<sub>2</sub> reduction on gas-diffusion electrodes and why catalytic  
12  
13 performance must be assessed at commercially-relevant conditions. *Energy Environ. Sci.* **2019**, *12*  
14  
15 (5), 1442-1453.  
16  
17  
18  
19 53. Zhang, F.; Co, A. C., Direct Evidence of Local pH Change and the Role of Alkali Cation  
20  
21 during CO<sub>2</sub> Electroreduction in Aqueous Media. *Angew. Chem. Int. Ed.* **2020**, *59* (4), 1674-1681.  
22  
23  
24  
25 54. Singh, M. R.; Kwon, Y.; Lum, Y.; Ager, J. W.; Bell, A. T., Hydrolysis of Electrolyte  
26  
27 Cations Enhances the Electrochemical Reduction of CO<sub>2</sub> over Ag and Cu. *J. Am. Chem. Soc.* **2016**,  
28  
29 *138* (39), 13006-13012.  
30  
31  
32  
33 55. Barsotti, R. J.; Vahey, M. D.; Wartena, R.; Chiang, Y. M.; Voldman, J.; Stellacci, F.,  
34  
35 Assembly of metal nanoparticles into nanogaps. *Small* **2007**, *3* (3), 488-499.  
36  
37  
38  
39 56. Arulmozhi, N.; P Hersbach, T. J.; M Koper, M. T., Nanoscale morphological evolution of  
40  
41 monocrystalline Pt surfaces during cathodic corrosion. *PNAS* **2017**, *117* (51), 32267-32277.  
42  
43  
44  
45 57. Boettcher, S. W.; Strandwitz, N. C.; Schierhorn, M.; Lock, N.; Lonergan, M. C.; Stucky,  
46  
47 G. D., Tunable electronic interfaces between bulk semiconductors and ligand-stabilized  
48  
49 nanoparticle assemblies. *Nat. Mater.* **2007**, *6* (8), 592-596.  
50  
51  
52  
53  
54  
55  
56  
57  
58  
59  
60

- 1  
2  
3 58. Chuang, C.-H. M.; Brown, P. R.; Bulović, V.; Bawendi, M. G., Improved performance and  
4 stability in quantum dot solar cells through band alignment engineering. *Nat. Mater.* **2014**, *13* (8),  
5 796-801.  
6  
7  
8  
9  
10  
11 59. Kramer, I. J.; Sargent, E. H., The Architecture of Colloidal Quantum Dot Solar Cells:  
12 Materials to Devices. *Chem. Rev.* **2013**, *114* (1), 863-882.  
13  
14  
15  
16  
17 60. Bernechea, M.; Miller, N. C.; Xercavins, G.; So, D.; Stavrinadis, A.; Konstantatos, G.,  
18 Solution-processed solar cells based on environmentally friendly AgBiS<sub>2</sub> nanocrystals. *Nat.*  
19 *Photonics* **2016**, *10* (8), 521-525.  
20  
21  
22  
23  
24 61. Pander, J. E.; Ren, D.; Yeo, B. S., Practices for the collection and reporting of  
25 electrocatalytic performance and mechanistic information for the CO<sub>2</sub> reduction reaction. *Catal.*  
26 *Sci. Technol.* **2017**, *7* (24), 5820-5832.  
27  
28  
29  
30  
31  
32 62. Kittel, C., Chapter 3 - Crystal Binding and Elastic Constants. *Introduction to Solid State*  
33 *Physics* **2004**, 453-486.  
34  
35  
36  
37  
38 63. King, D. A., Surface Diffusion of Adsorbed Species: A Review. *J. Vac. Sci. Technol.* **1979**,  
39 *17* (1), 241-247.  
40  
41  
42  
43 64. Morris, M. A.; Barnes, C. J.; King, D. A., Monolayer and multilayer surface diffusion,  
44 growth mode and thermal stability of indium on W {100}. *Surf. Sci.* **1986**, *173* (2-3), 618-638.  
45  
46  
47  
48  
49 65. King, D. A., Surface diffusion of adsorbed species: A review. *J. Vac. Sci. Technol.* **1998**,  
50 *17* (1), 241-241.  
51  
52  
53  
54  
55  
56  
57  
58  
59  
60

1  
2  
3 66. Wagner, M.; Seiler, S.; Meyer, B.; Boatner, L. A.; Schmid, M.; Diebold, U., Reducing the  
4  
5 In<sub>2</sub>O<sub>3</sub>(111) Surface Results in Ordered Indium Adatoms. *Adv. Interfaces* **2014**, *1* (8), 1400289-  
6  
7 1400289.  
8  
9

10  
11 67. Wei, H. L.; Zhang, L.; Liu, Z.; Huang, H.; Zhang, X., Spontaneous growth of indium  
12  
13 nanostructures. *J. Cryst. Growth* **2006**, *297* (2), 300-305.  
14  
15  
16  
17  
18  
19  
20  
21  
22  
23  
24  
25  
26  
27  
28  
29  
30  
31  
32  
33  
34  
35  
36  
37  
38  
39  
40  
41  
42  
43  
44  
45  
46  
47  
48  
49  
50  
51  
52  
53  
54  
55  
56  
57  
58  
59  
60

For Review Only

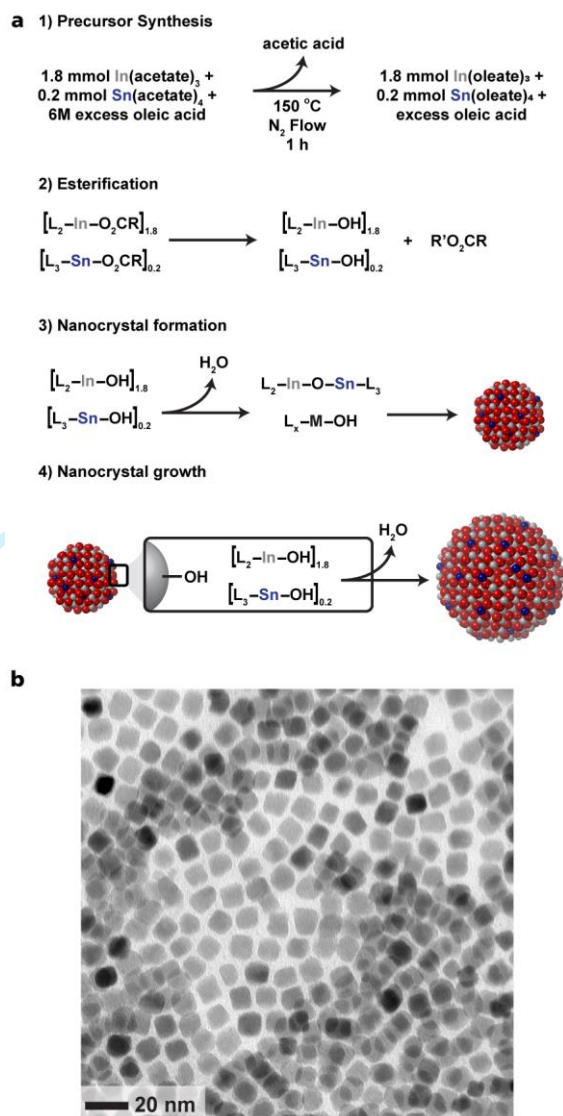


**Figure 1.** (a) Schematic depiction of the mechanism of ITO nanocrystal formation. (b) TEM image of the oleate-stabilized ITO nanocrystals used in this study (prior to annealing).

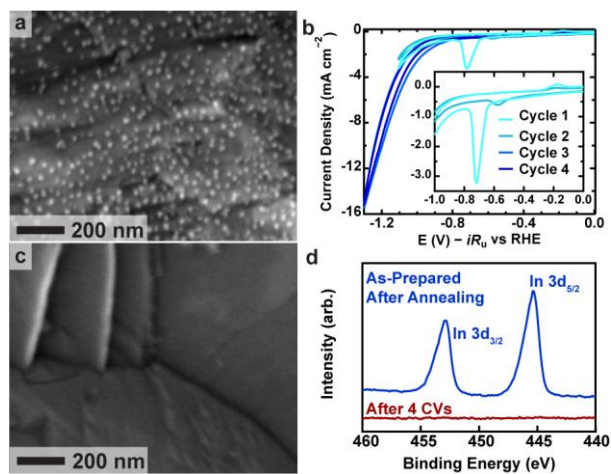


**Figure 2.** (a) SEM image of the as-prepared electrode. (b) Cyclic voltammograms (CVs) of a BDD electrode containing approximately one monolayer of ITO nanocrystals conducted in Ar-saturated 0.5 M  $\text{KHCO}_3$ . (c) SEM image of the BDD electrode after four CV cycles. (d) XPS analysis of the In 3d region conducted on the as-prepared electrode (blue) and the electrode after performing four CVs in Ar-sparged 0.5 M  $\text{KHCO}_3$ .

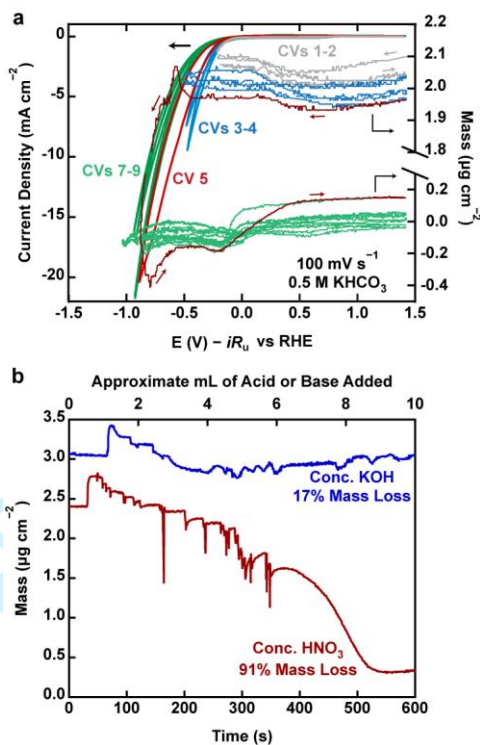


**Figure 3.** QCM data of ITO films under various conditions. (a) Mass loss from an ITO nanocrystal film deposited on a QCM crystal as a function of applied potential. Several CVs were performed in 0.5 M KHCO<sub>3</sub> from open circuit voltage (1.48 V vs RHE) to -0.14 V (gray), -0.50 V (blue), and -0.96 V (red and green) vs RHE. Colored arrows show the CV sweep direction. (b) Mass monitored as a function of amount of concentrated HNO<sub>3</sub> (red) or KOH (blue) added to an ultrapure water solution containing the QCM electrode.

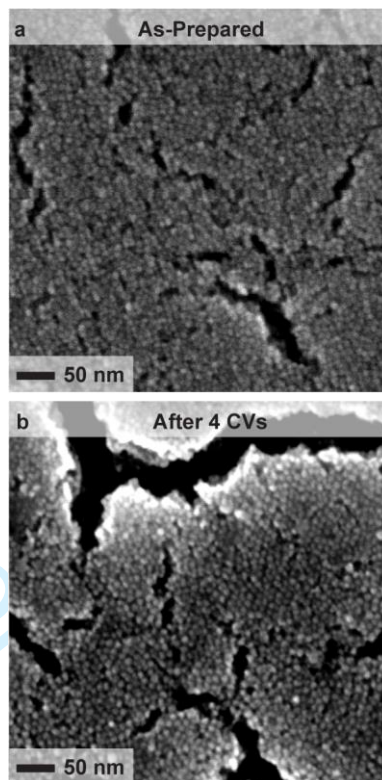


**Figure 4.** SEM images of an ITO nanocrystal film deposited on a BDD electrode from a  $50 \text{ mg mL}^{-1}$  nanocrystal solution (after annealing) (a) before, and (b) after performing four CVs of the electrode. CVs were performed in Ar-saturated  $0.5 \text{ M KHCO}_3$ .

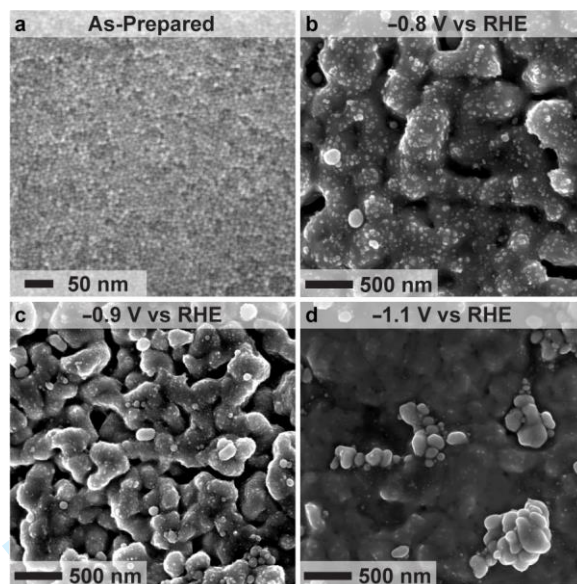


**Figure 5.** SEM images of ITO nanocrystal films (a) as-prepared, and after applying (b) -0.8, (c) -0.9, and (d) -1.1 V vs RHE for 80 min in CO<sub>2</sub>-saturated 0.5 M KHCO<sub>3</sub>. In all the panels the underlying electrode is not visible and the observed features are ascribed to catalyst agglomerates.

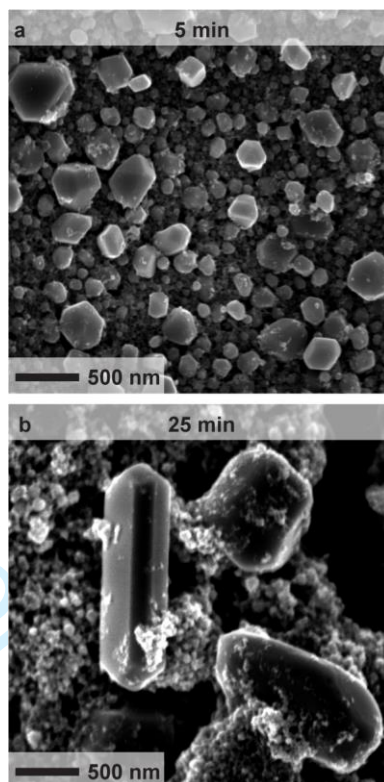


**Figure 6.** SEM images of ITO nanocrystal film after applying  $-1.1$  V vs RHE in  $\text{CO}_2$ -sparged  $0.5$  M  $\text{KHCO}_3$  electrolyte for (a) 5 min and (b) 25 min.